

# Conservative finite volume schemes for the quasi-geostrophic equation on coastal-conforming unstructured primal-dual meshes

Qingshan Chen · Lili Ju

March 1, 2022

**Abstract** In this paper we propose finite volume schemes for solving the inviscid and viscous quasi-geostrophic equations on coastal-conforming unstructured primal-dual meshes. Several approaches for enforcing the boundary conditions are also explored along with these schemes. The pure transport part in these schemes are shown to conserve the potential vorticity along fluid paths in an averaged sense, and conserve the potential enstrophy up to the time truncation errors. Numerical tests based on the centroidal Voronoi-Delaunay meshes are performed to confirm these properties, and to distinguish the dynamical behaviors of these schemes. Finally some potential applications of these schemes in different situations are discussed.

**Keywords** Quasi-geostrophic equation; finite volume method; unstructured primal-dual meshes; vorticity-divergence formulation

## 1 Introduction

Due to the inherent instabilities of large-scale geophysical flows, i.e. the ocean and atmosphere, numerical simulations of these flows cease to be a reliable reflection of the reality in the pointwise sense after a few days. Then, it is natural that simulations of large-scale geophysical flows set their goal on capturing the long-term dynamics of these flows in the statistical sense. Numerical schemes are thus developed with this goal in mind. The best known class of

---

Q. Chen  
Department of Mathematical Sciences  
Clemson University  
E-mail: qsc@clemson.edu

L. Ju  
Department of Mathematics  
University of South Carolina  
E-mail: ju@math.sc.edu

schemes are the staggered-grid schemes of Arakawa and Lamb ([1]). Among this class of schemes, the most popular and the most widely used one is the so-called C-grid scheme, for its excellent representation of the inertial-gravity waves. The C-grid scheme, also known as the MAC scheme in the classical CFD community ([15]), specifies the scalar quantities, such as the mass and pressure, at cell centers, and the *normal* velocity components at the cell edges. In the simulations, the tangential velocity components are needed as well, due to the nonlinearity within the models. In the original settings of rectangular meshes for the C-grid or MAC schemes, the tangential velocity components can be easily reconstructed from the normal velocity components. However, when the C-grid scheme is implemented on unstructured meshes, the reconstruction becomes a non-trivial matter, and is a significant source of errors (see [29, 32, 33]). One of the authors of this present paper (Q.C.) made an attempt to remedy such reconstruction issue by specifying both the normal and tangential velocity components on the edges ([7], and it has been shown that, for the linearized shallow water equations with a constant Coriolis force, the resulting scheme is decoupled on the primary and dual meshes ([4]).

Another type of numerical scheme that outperforms the C-grid in resolving inertial-gravity waves is the non-staggered Z-grid scheme ([24]). Indeed, it is clear that the Z-grid scheme possesses the optimal dispersive wave relations among second-order numerical schemes. The Z-grid scheme collocates the mass, vorticity, and the divergence at the cell centers. Both the normal and tangential velocity components can be recovered from the vorticity and divergence by solving some Poisson equations over the dual one of the primary-dual mesh. Thus, the tricky reconstruction issue is avoided, at the cost of inverting some Laplace operators. The Z-grid scheme has been implemented for the shallow water equations on icosahedral meshes on a global sphere by Heikes and Randall ([17, 16]). The cost issue associated with inverting the Laplace operator on a global sphere was dealt by a multi-grid technique. However, we have not seen any numerical and analytic studies of that scheme on bounded unstructured meshes.

We aim to adapt the Z-grid scheme for simulations of more general oceanic flows over bounded domains. Our choice of the Z-grid scheme is based on two factors. The first factor, an obvious one, is already mentioned in above, that is, its optimal representation of the dispersive wave relations. The second factor, which is equally important, if not more so, is that the use of vorticity and divergence as prognostic variables enable more accurate simulations of these fundamental quantities of fluid dynamics. Due to the inherent irregularities on unstructured meshes, the commonly used finite difference and finite volume schemes on these meshes are only between first and second-order accurate. For momentum-based numerical schemes, this means that there is only a low, or even no accuracy for quantities that are higher order derivatives of the momentum.

In order to harness the great potentials of the Z-grid schemes, several outstanding issues need to be addressed. The first issue concerns the boundary conditions (BCs). For the momentum based systems and schemes, the no-flux

or no-slip BCs on the velocity are the natural choices. But these natural choices do not have any counterparts on the vorticity or divergence variables. The second issue concerns the specifications of the diagnostic variables to ensure the proper transport and/or conservation of certain quantities such as the potential vorticity. Heikes and Randall ([16]) only partially solved this issue for the icosahedral meshes and special types of flows. Lastly, in order for the vorticity-divergence based schemes to be appealing for practical applications, its efficiency needs to be improved, and be brought closer to, or on par with that of the momentum-based numerical schemes.

A large-scale geophysical flow such as the ocean or atmosphere is an extremely complex dynamical system that exhibits a wide spectrum of spatial and temporal scales and highly nonlinear phenomena. Developing a reliable and efficient vorticity-divergence based numerical scheme for this system demands careful planning and systematic efforts. Our plan is to utilize a hierarchy of models that have already been proposed for large-scale geophysical flows, and develop, implement, study, and test vorticity-divergence based schemes for these models, starting from simple models, and progressing to more complex and more realistic ones. In this work, we deal with the barotropic quasi-geostrophic (QG) equation. More complex models, such as the shallow water equations, will be considered in the subsequent works.

The barotropic QG equation captures the dynamics of large-scale geophysical flows in a single scalar equation that describes the evolution of the QG potential vorticity (PV). It is the model developed and used by Charney for the very first numerical weather prediction on an electronic computer ([3]). The QG equation is already in a vorticity based form, and the velocity field for the QG, as the leading component of the full velocity field, is divergence free. For numerical simulation of the QG on an arbitrary bounded domain, the most pressing question is how to handle the boundary conditions. The question will be one of the main focuses of the current work. We will explore the proper setups for the inviscid and viscous models. We will also explore the difference and connection between artificial BC's, and implicitly and explicitly enforced BC's. The QG equation is relatively simple compared with other models, and therefore the specification or computation of the diagnostics (e.g. the stream function, the velocity field) are mostly straightforward. Under the numerical setting and discretization techniques that we choose in this paper, we are able to show the pure advection part of our schemes conserve the potential enstrophy up to time truncation error, and conserve the PV along the fluid paths in an averaged sense. The third issue, namely efficiency, will be left for future works, partly due to the fact that the QG is already in a vorticity-based form, and there is not any momentum-based numerical scheme for us to compare to.

We also note that a key part of the ingredients for our success in handling the BC's and the accuracy and conservation of the potential enstrophy and the PV is use of the coastal-conforming centroidal Voronoi-Delaunay mesh that we choose as the primal-dual mesh for the numerical simulations. Centroidal Voronoi tessellation (CVT) or spherical CVT (SCVT) with their dual Delaunay triangulations have been adopted for oceanic and atmospheric modeling

by the MPAS (“Model for Prediction Across Scales”) team ([27, 26, 28, 18, 30]). The C-grid staggering techniques are used, and the scalar quantities, such as mass, are specified at the Voronoi cell centers, because the Voronoi cells, which are mostly hexagonal, are more accommodating to the wave propagations compared with the dual triangular cells ([9, 14]). Meshes for bounded ocean basins are culled out of meshes on the global sphere. Meshes generated in this fashion are almost guaranteed to have non-smooth boundaries: every connected boundary edges form an angle of approximately  $120^\circ$ , as they are the edges of (mostly) hexagonal cells. This type of meshes will present an even more serious complication for the vorticity-divergence based numerical schemes, because the cell-centered scalar quantities such as the vorticity, divergence, and stream functions, are always away from the boundary. For these reasons, we take a different bottom-up approach. Meshes will be generated for the ocean basins directly, with the boundary fitted with partial Voronoi cells (or dual triangular cells). With this approach, we are able to obtain a smooth fitting to the coastal line, and have nodal points, where certain scalar quantities are defined, on the boundary directly. On this mesh, a complete discrete vector field theory has been developed ([5]), which aides the subsequent development and analysis of the numerical schemes.

The rest of the paper is organized as follows. In Section 2 we recall the barotropic QG equation and its theoretically required boundary conditions and constraints. In Section 3 the specifications of the mesh are provided, and the main results of the discrete vector field theory on this type of meshes are recalled. In Section 4, some finite volume schemes, for both the inviscid and viscous models, are presented. Analyses of the transport part of the schemes concerning its conservation of the PV and the potential enstrophy are carried out in Section 5. Numerical tests and comparisons of these schemes to demonstrate their qualitative behaviors are given in Section 6. Concluding remarks and some potential applications of these schemes in different situations are finally given in Section 7.

## 2 The continuous model and the boundary conditions

The barotropic QG equation reads

$$\frac{\partial}{\partial t}q + \mathbf{u} \cdot \nabla q = \frac{1}{H} \nabla \times \boldsymbol{\tau} - \alpha \zeta + \mu \Delta \zeta, \quad (1a)$$

$$q = \zeta + \beta y - \frac{f_0}{H}(\psi - b), \quad (1b)$$

$$\mathbf{u} = \frac{g}{f_0} \nabla^\perp \psi, \quad (1c)$$

$$\zeta = \nabla \times \mathbf{u} \equiv \frac{g}{f_0} \Delta \psi. \quad (1d)$$

In the above,  $q$  stands for the potential vorticity,  $\zeta$  the relative vorticity, and  $\mathbf{u}$  the horizontal velocity field, and  $\psi$  the stream function. The parameter  $f_0$

represents the average Coriolis parameter,  $\beta$  (the beta term) the meridional changing rate of the Coriolis parameter,  $g$  the gravity,  $b$  the bottom topography, and  $H$  the average fluid depth. The friction with the bottom of the domain leads to a zeroth order damping to the vorticity field, as revealed by the asymptotic analysis that produces the QG model ([23]). The strength of the damping is parameterized by  $\alpha$  on the right-hand side of (1a). The lateral friction leads to a second-order damping to the vorticity field, in the form of the Laplacian, as expected. The strength of the lateral damping is parameterized by  $\mu$ . The vector field  $\boldsymbol{\tau}$  represents the only external forcing to the system, which is the wind in the physical world.

The potential vorticity  $q$  is a scalar quantity that is being transported by the velocity field  $\mathbf{u}$ , and they are related through the stream function  $\psi$  via (1b), (1c) and (1d). In this sense, the potential vorticity can be considered an active tracer ([13]). Within the specification (1b) for the PV, the zero order term  $\psi$  represents the impact on the vorticity from the fluctuations of the top surface. The fluctuations of the top surface is usually small, and thus this term is often omitted from the QG equation ([22]). However, in the interior of the geophysical flows, where the interior Rossby deformation radius is on the same order as the flow length scale, the interface deforms much more easily, and thus is a major contributor to the vorticity ([23]). For this reason, we include the top surface fluctuation in our study.

On a bounded domain  $\mathcal{M}$ , boundary conditions are required to complete the system (1). When the lateral friction is absent, we consider the no-flux boundary condition, which is the most natural choice for a bounded domain surrounded by non-penetrable walls,

$$\mathbf{u} \cdot \mathbf{n} = 0, \quad \text{on } \partial\mathcal{M}. \quad (2)$$

where  $\mathbf{n}$  represents the outer normal unit vector on the boundary  $\partial\mathcal{M}$ . In terms of the stream function  $\psi$ , this conditions means that

$$\frac{\partial\psi}{\partial\mathbf{t}} = 0 \quad \text{or} \quad \psi = \text{constant}, \quad \text{on } \partial\mathcal{M}, \quad (3)$$

where  $\mathbf{t}$  represents the positively oriented unit tangential vector along the boundary  $\partial\mathcal{M}$ . When the lateral friction is present, additional constraints are required. In the context of a closed domain, the most natural choice is the non-slip boundary condition,

$$\mathbf{u} \cdot \mathbf{t} = 0, \quad \text{on } \partial\mathcal{M}. \quad (4)$$

In terms of the stream function  $\psi$ , this conditions means that

$$\frac{\partial\psi}{\partial\mathbf{n}} = 0, \quad \text{on } \partial\mathcal{M}. \quad (5)$$

A key step, in both the theoretical analysis and the numerical computation of the QG equation is to recover the stream function  $\psi$  from the potential vorticity  $q$ . The procedure for recovering the streamfunction varies, depending on whether the friction is present or not.

## 2.1 Without lateral friction

When the lateral friction is absent, the stream function  $\psi$  satisfies the elliptic equation (1b) and the no-flux BC's (3). Compared with the standard elliptic BVP with Dirichlet BC's, this system still has one parameter to be determined, namely, the constant value of  $\psi$  along the boundary. We note that boundary value can not be arbitrarily set, due to the zeroth order term on the right-hand side of (1b). An additional constraint is needed in order to determine the constant value of  $\psi$  along the boundary. A logical option is the mass conservation constraint,

$$\int_{\mathcal{M}} \psi dx = 0. \quad (6)$$

Hence, in the inviscid case, the stream function  $\psi$  is the solution to a non-standard elliptic boundary value problem (BVP),

$$\zeta + \beta y - \frac{f_0}{H}(\psi - b) = q, \quad \text{in } \mathcal{M}, \quad (7a)$$

$$\psi = l, \quad \text{on } \partial\mathcal{M}, \quad (7b)$$

$$\int_{\mathcal{M}} \psi dx = 0. \quad (7c)$$

The solvability of this non-standard elliptic BVP and the uniqueness of its solution have been addressed in detail in [6]. Here, we recall the basic strategy, since it has bearing on the numerical computation as well. We let  $\psi_1$  and  $\psi_2$  be solutions of the following elliptic BVPs, respectively,

$$\frac{g}{f_0} \Delta \psi_1 - \frac{f_0}{H} \psi_1 = q - \beta y - \frac{f_0}{H} b, \quad \text{in } \mathcal{M}, \quad (8a)$$

$$\psi_1 = 0, \quad \text{on } \partial\mathcal{M}, \quad (8b)$$

and

$$\frac{g}{f_0} \Delta \psi_2 - \frac{f_0}{H} \psi_2 = 0, \quad \text{in } \mathcal{M}, \quad (9a)$$

$$\psi_2 = 1, \quad \text{on } \partial\mathcal{M}. \quad (9b)$$

By the standard elliptic PDE theories, both BVPs (8) and (9) are well-posed under proper assumptions on the forcing on the right-hand side of (8a) and on the domain  $\mathcal{M}$ . The solution to the original BVP (7) can be expressed in terms of  $\psi_1$  and  $\psi_2$ ,

$$\psi = \psi_1 + l\psi_2. \quad (10)$$

The unknown constant  $l$  can be determined using the mass conservation constraint (7c)

$$\int_{\mathcal{M}} \psi dx = \int_{\mathcal{M}} \psi_1 dx + l \int_{\mathcal{M}} \psi_2 dx = 0,$$

which leads to

$$l = - \frac{\int_{\mathcal{M}} \psi_1 dx}{\int_{\mathcal{M}} \psi_2 dx}. \quad (11)$$

We would like to point out that the expression (11) for  $l$  is valid because, as a consequence of the maximum principle,  $\psi_2$  is positive in the interior of the domain, and the integral  $\int_{\mathcal{M}} \psi_2 dx$  in the denominator of (11) is strictly positive.

The well-posedness of a frictionless (i.e., no bottom drag or lateral diffusion) version of the model (1) with the BC (7b) and the constraint (7c) has been established in [6].

## 2.2 With lateral friction

When the lateral friction is present, both the no-flux and the no-slip boundary conditions (3) and (5) apply, however these conditions are over-specified for a second-order elliptic equation (1b). To obtain a well-posed system, one can apply the Laplacian operator  $\Delta$  to (1b) to get a fourth-order biharmonic equation,

$$\frac{g}{f_0} \Delta^2 \psi - \frac{f_0}{H} \Delta \psi = q - \frac{f_0}{H} \Delta b. \quad (12)$$

The solution to the system (12), (3) and (5) is not unique, since if  $\psi$  is a solution, then so is  $\psi + c$  for any constant  $c$ . To fix this arbitrariness, one can set  $\psi = 0$  on the boundary. Doing so will not affect the shape of the stream function, and hence the velocity field, but it contradicts the assumption of a free top surface. A better option is again to enforce the mass conservation constraint (6).

Hence, in the case with lateral friction, one can determine the stream function from the PV by solving a fourth-order BVP,

$$\left\{ \begin{array}{ll} \frac{g}{f_0} \Delta^2 \psi - \frac{f_0}{H} \Delta \psi = q - \frac{f_0}{H} \Delta b, & \text{in } \mathcal{M}, \\ \frac{\partial \psi}{\partial \mathbf{t}} = 0, & \text{on } \partial \mathcal{M}, \\ \frac{\partial \psi}{\partial \mathbf{n}} = 0, & \text{on } \partial \mathcal{M}, \\ \int_{\mathcal{M}} \psi dx = 0. \end{array} \right. \quad (13)$$

However, dynamically, this approach for determining the stream function  $\psi$  is defective. The beta term is a dominant term in the QG dynamics. But, as a linear function, the beta term falls into the null space of the Laplace operator  $\Delta$ . As a consequence, when the Laplacian operator is applied to the original elliptic equation, the beta term completely disappears. In the next section, we will explore alternative approaches for numerically determining the stream function  $\psi$  when the lateral friction is present.

### 3 Mesh specification and the discrete vector field theory

#### 3.1 Mesh specification

Our schemes for the QG equation on based on very general orthogonal dual meshes, with one called *primal* and the other *dual*. The meshes consist of polygons, called cells, of arbitrary shape. To avoid potential technical issues with the boundary, we assume that the domain  $\mathcal{M}$  itself is also polygonal. The centers of the cells on the primal mesh are the vertices of the cells on the dual mesh, and vice versa. The edges of the primary cells intersect *orthogonally* with the edges of the dual cells. The line segments of the boundary  $\partial\mathcal{M}$  pass through the centers of the primary cells that border the boundary (Figure 3). Thus primary cells on the boundary can be viewed as slices of regular cells like those in the interior of the domain. Two examples of this type of boundary conforming primal-dual meshes are shown in Figure 1.

**Table 1** Sets of basic mesh elements.

Set	Definition
$\mathcal{IC}$	Set of interior cells
$\mathcal{BC}$	Set of boundary cells
$\mathcal{IE}$	Set of interior edges
$\mathcal{BE}$	Set of boundary edges
$\mathcal{V}$	Set of vertices

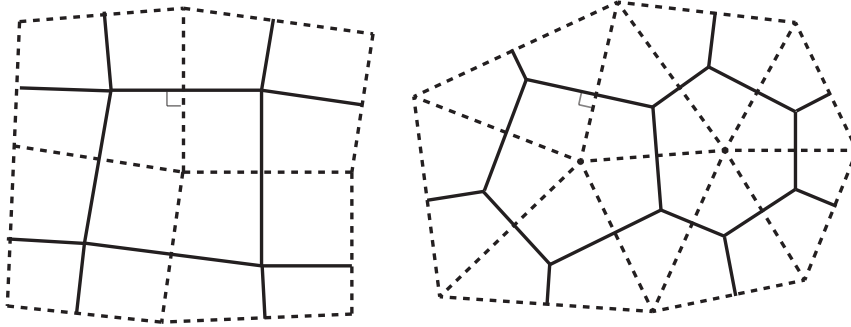


**Fig. 1** Generic conforming primal-dual meshes with the domain boundary passing through the primary cell centers, where the dark line denotes the primal mesh and the dashed line the dual mesh. Left: a generic quadrilateral dual mesh; right: a generic Voronoi-Delaunay mesh.



In order to effectively describe the schemes on these meshes, some notations are in order, for which we follow the conventions made in [7, 29]. The diagram in Figure 2 represents a Voronoi-Delaunay mesh element. The primary cells are denoted as  $A_i$ ,  $1 \leq i \leq N_c + N_{cb}$ , where  $N_c$  denotes the number of cells that are in the interior of the domain, and  $N_{cb}$  the number of cells that are on the boundary. The dual cells, which all lie inside the domain, are denoted as  $A_\nu$ ,  $1 \leq \nu \leq N_v$ . The area of  $A_i$  (resp.  $A_\nu$ ) is denoted as  $|A_i|$  (resp.  $|A_\nu|$ ). Each primary cell edge corresponds to a distinct dual cell edge, and vice versa. Thus the primary and dual cell edges share a common index  $e$ ,  $1 \leq e \leq N_e + N_{eb}$ , where  $N_e$  denotes the number of edge pairs that lie entirely in the interior of the domain, and  $N_{eb}$  the number of edge pairs on the boundary. Upon an edge pair  $e$ , the distance between the two primary cell centers, which is also the length of the corresponding dual cell edge, is denoted as  $d_e$ , while the distance between the two dual cell centers, which is also the length of the corresponding primary cell edge, is denoted as  $l_e$ . These two edges form the diagonals of a diamond-shaped region, whose vertices consist of the two neighboring primary cell centers and the two neighboring dual centers. The diamond-shaped region is also indexed by  $e$ , and will be referred to as  $A_e$ . The Euler formula for planar graphs states that the number of primary cell centers  $N_c + N_{cb}$ , the number of vertices (dual cell centers)  $N_v$ , and the number of primary or dual cell edges  $N_e + N_{eb}$  must satisfy the relation

$$N_c + N_{cb} + N_v = N_e + N_{eb} + 1. \quad (14)$$

The sets of basic elements (cells, edges, etc) are given in Table 1. Additional sets of elements, which define the connectivity of the primal-dual mesh, are given in Table 2.

**Table 2** Sets of elements defining the connectivity of a unstructured primal-dual mesh.

Set	Definition
$\mathcal{EC}(i)$	Set of edges on the primary cell $A_i$
$\mathcal{VC}(i)$	Set of dual cells on the primary cell $A_i$
$\mathcal{CE}(e)$	Set of primary cells on the edge $e$
$\mathcal{VE}(e)$	Set of dual cells on the edge $e$
$\mathcal{CV}(\nu)$	Set of primary cells on the dual cell $D_\nu$
$\mathcal{EV}(\nu)$	Set of edges on the dual cell $D_\nu$

For each edge pair, a unit vector  $\mathbf{n}_e$ , normal to the primary cell edge, is specified. A second unit vector  $\mathbf{t}_e$  is defined as

$$\mathbf{t}_e = \mathbf{k} \times \mathbf{n}_e, \quad (15)$$

with  $\mathbf{k}$  standing for the upward unit vector. Thus  $\mathbf{t}_e$  is orthogonal to the dual cell edge, but tangent to the primary cell edge, and points to the vertex on

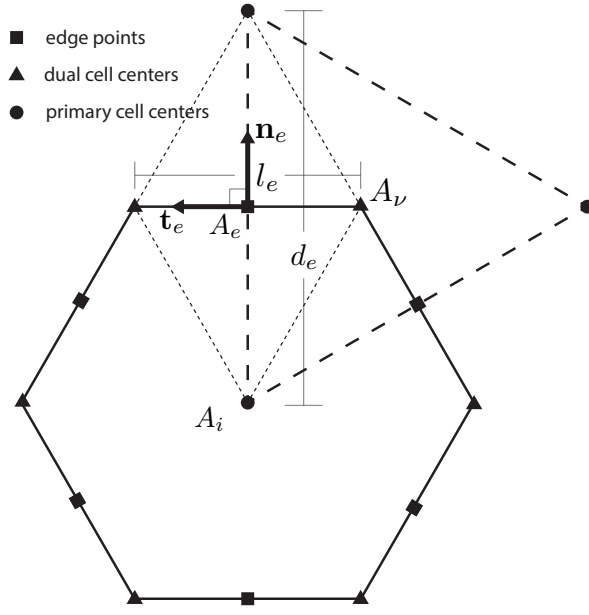


**Fig. 2** Notations of a Voronoi-Delaunay mesh element.

the left side of  $\mathbf{n}_e$ . For each edge  $e$  and for each  $i \in \mathcal{CE}(e)$  (the set of cells on edge  $e$ , see Table 2), we define the direction indicator

$$n_{e,i} = \begin{cases} 1 & \text{if } \mathbf{n}_e \text{ points away from primary cell } A_i, \\ -1 & \text{if } \mathbf{n}_e \text{ points towards primary cell } A_i, \end{cases} \quad (16)$$

and for each  $\nu \in \mathcal{VE}(e)$ ,

$$t_{e,\nu} = \begin{cases} 1 & \text{if } \mathbf{t}_e \text{ points away from dual cell } A_\nu, \\ -1 & \text{if } \mathbf{t}_e \text{ points towards dual cell } A_\nu. \end{cases} \quad (17)$$

For this study, we make the following regularity assumptions on the meshes. We assume that the diamond-shaped region  $A_e$  is actually convex. In other words, the intersection point of each edge pair falls inside each of the two edges. We also assume that the meshes are quasi-uniform, in the sense that there exists  $h > 0$  such that, for each edge  $e$ ,

$$mh \leq l_e, d_e \leq Mh \quad (18)$$

for some fixed constants  $(m, M)$  that are independent of the meshes. The staggered dual meshes are thus designated by  $\mathcal{T}_h$ . For the convergence analysis, it is assumed in [5] that, for each edge pair  $e$ , the primary cell edge nearly bisect the dual cell edge, and miss by at most  $O(h^2)$ . This assumption is also made here for the error analysis. Generating meshes satisfying this requirement on

irregular domains, i.e. domains with non-smooth boundaries or domains on surfaces, can be a challenge, and will be addressed elsewhere. But we point out that, on regular domains with smooth boundaries, this type of meshes can be generated with little extra effort in addition to the use of standard mesh generators, such as the centroidal Voronoi tessellation (CVT) or Spherical CVT (SCVT) meshing algorithm ([12, 11, 10]).

### 3.2 Specification of the discrete differential operators

In this section, we denote by  $\psi_h$  a discrete scalar field defined at the primary cell centers, and by  $\tilde{\varphi}_h$  a discrete scalar field defined at the primary cell vertices,

$$\begin{aligned}\psi_h &= \sum_{i \in \mathcal{IC} \cup \mathcal{BC}} \psi_i \chi_i, \\ \tilde{\varphi}_h &= \sum_{\nu \in \mathcal{IC} \cup \mathcal{BC}} \tilde{\varphi}_\nu \chi_\nu.\end{aligned}$$

Here,  $\chi_i$  and  $\chi_\nu$  stand for the piecewise constant characteristic functions on the primary cells and on the dual cells, respectively. A discrete scalar field on the primary mesh can be mapped to a discrete scalar field on the dual mesh via area-weighted averaging,

$$\tilde{\psi}_\nu = [\widetilde{\psi_h}]_\nu \equiv \frac{1}{|A_\nu|} \sum_{i \in \mathcal{CV}(\nu)} \psi_i |A_{i,\nu}|. \quad (19)$$

In the above,  $|A_{i,\nu}|$  stands for the area of the kite-shaped region between cell  $i$  and vertex  $\nu$  (see Figure 2). A discrete scalar field on the primary mesh can also be mapped to a discrete scalar field on the edges via arithmetic mean,

$$\hat{\psi}_e = [\widehat{\psi_h}]_e \equiv \frac{1}{2} \sum_{i \in \mathcal{CE}_e} \psi_i. \quad (20)$$

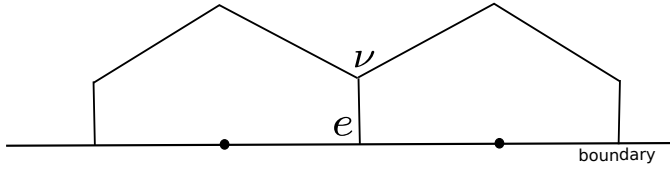


**Fig. 3** With each (partial) edge on the boundary, only one vertex is associated.

On each edge  $e$ , the discrete gradient operator on  $\psi_h$  is defined as

$$[\nabla_h \psi_h]_e = \frac{-1}{d_e} \sum_{i \in \mathcal{CE}(e)} \psi_i n_{e,i}, \quad (21)$$

and the skewed discrete gradient operator on  $\tilde{\varphi}_h$  is defined as

$$[\tilde{\nabla}_h^\perp \tilde{\varphi}_h]_e = \frac{1}{l_e} \sum_{\nu \in \mathcal{VE}(e)} \tilde{\varphi}_\nu t_{e,\nu}. \quad (22)$$

With each boundary edge  $e$ , since only one vertex is associated (Figure 3), the definition (22) can be written as

$$[\tilde{\nabla}_h^\perp \tilde{\varphi}_h]_{e \text{ on boundary}} = \frac{1}{l_e} \tilde{\varphi}_\nu t_{e,\nu}, \quad (23)$$

where  $\nu$  is the single element in  $\mathcal{VE}(e)$ . This amounts to implicitly requiring that  $\tilde{\varphi}_h$  vanishes on the boundary. We define the gradient of  $\psi_h$  and the skew gradient of  $\tilde{\varphi}_h$  as

$$\nabla_h \psi_h = \sum_{e=1}^{N_e+N_{eb}} [\nabla_h \psi_h]_e \chi_e \mathbf{n}_e, \quad (24)$$

$$\tilde{\nabla}_h^\perp \tilde{\varphi}_h = \sum_{e=1}^{N_e+N_{eb}} [\tilde{\nabla}_h^\perp \tilde{\varphi}_h]_e \chi_e \mathbf{n}_e. \quad (25)$$

Here  $\chi_e$  represents the piecewise constant characteristic function on the diamond-shaped regions  $A_e$ .

We denote by  $\mathbf{u}_h$  and  $\mathbf{v}_h$  discrete vector fields defined at the edges, in the normal (w.r.t. the primary cells) and the tangential directions, respectively,

$$\begin{aligned} \mathbf{u}_h &= \sum_{e \in \mathcal{IE} \cup \mathcal{BE}} u_e \mathbf{n}_e \chi_e, \\ \mathbf{v}_h &= \sum_{e \in \mathcal{IE} \cup \mathcal{BE}} v_e \mathbf{t}_e \chi_e. \end{aligned}$$

Around each primary cell  $i$ , a discrete divergence operator can be defined on the discrete vector field  $\mathbf{u}_h$ ,

$$[\nabla_h \cdot \mathbf{u}_h]_i = \frac{1}{A_i} \sum_{e \in \mathcal{EC}(i)} u_e l_e n_{e,i}. \quad (26)$$

It is worth noting that, on partial cells on the boundary, the summation on the right-hand side only includes fluxes across the edges that are inside the domain and the partial edges that intersect with the boundary, and this amounts to imposing a no-flux condition across the boundary, i.e.  $\mathbf{u} \cdot \mathbf{n} = 0$  on  $\partial\mathcal{M}$ . It is clear from the definition (26) that the image of the discrete divergence operator  $\nabla_h \cdot$  on  $\mathbf{u}_h$  is a scalar field on the primary mesh, which can be written as

$$\nabla_h \cdot \mathbf{u}_h = \sum_{i \in \mathcal{IC} \cup \mathcal{BC}} [\nabla_h \cdot \mathbf{u}_h]_i \chi_i. \quad (27)$$

Around each dual cell  $\nu$ , a discrete curl operator can be defined on  $\mathbf{u}_h$ ,

$$\left[ \tilde{\nabla}_h \times \mathbf{u}_h \right]_\nu = \frac{-1}{A_\nu} \sum_{e \in \mathcal{EV}(\nu)} u_e d_e t_{e,\nu}. \quad (28)$$

The tilde atop  $\nabla$  again signifies the involvement of the dual cells. Thus, the image of the discrete curl operator  $\tilde{\nabla}_h \times$  on each  $\mathbf{u}_h$  is a scalar field defined on the dual mesh,

$$\tilde{\nabla}_h \times \mathbf{u}_h = \sum_{\nu=1}^{N_\nu} \left[ \tilde{\nabla}_h \times \mathbf{u}_h \right]_\nu \chi_\nu. \quad (29)$$

For a scalar field  $\psi_h$  defined at cell centers, the discrete Laplacian operator  $\Delta_h$  can also be defined,

$$\Delta_h \psi_h := \nabla_h \cdot (\nabla_h \psi_h) \quad (30)$$

Finally, in this study, we need an inner product for scalar fields on the primary mesh, and an inner product for discrete normal vector fields on the edges,

$$(\psi_h, \varphi_h)_{0,h} = \sum_{i \in \mathcal{IC} \cup \mathcal{BC}} \psi_i \varphi_i A_i, \quad (31)$$

$$(\mathbf{u}_h^1, \mathbf{u}_h^2)_{0,h} = \sum_{e \in \mathcal{IE} \cup \mathcal{BE}} u_e^1 u_e^2 A_e. \quad (32)$$

The discrete forms of the integration by parts formulas are also available.

**Lemma 1** *For the discrete normal vector field  $\mathbf{u}_h$  and the discrete scalar fields  $\psi_h$  and  $\tilde{\varphi}_h$ , the following relations hold:*

$$(\mathbf{u}_h, \nabla_h \psi_h)_{0,h} = -\frac{1}{2} (\nabla_h \cdot \mathbf{u}_h, \psi_h)_{0,h}, \quad (33)$$

$$\left( \mathbf{u}_h, \tilde{\nabla}_h^\perp \tilde{\varphi}_h \right)_{0,h} = -\frac{1}{2} \left( \tilde{\nabla}_h \times \mathbf{u}_h, \tilde{\varphi}_h \right)_{0,h}. \quad (34)$$

The proof can be found in [5]. We simply point out that these integration by parts formulas hold thanks to the no-flux boundary condition on  $\mathbf{u}_h$ , implied in the specification of the discrete divergence operator  $\nabla_h \cdot (\cdot)$ , and the homogeneous Dirichlet boundary condition on  $\tilde{\varphi}_h$ , implied in the specification of the skewed gradient operator  $\tilde{\nabla}_h^\perp$ .

## 4 Finite volume schemes for the QG equation

### 4.1 Finite volume schemes for the inviscid QG equation

We deal with the system (1), but with the viscosity  $\mu$  set to zero. The proper boundary conditions for the resulting system are the no-flux boundary condition (3) and the mass conservation constraint (6).

#### 4.1.1 A finite volume scheme for the inviscid QG equation (IVFV1)

The key quantity for the QG equation is the PV  $q$ . We approximate this quantity with a discrete scalar field  $q_h$  that is defined at cell centers, i.e.,

$$q_h = \sum_{i \in \mathcal{IC} \cup \mathcal{BC}} q_i \chi_i. \quad (35)$$

Closely related to the PV is the discrete stream function  $\psi_h$ , defined as

$$\psi_h = \sum_{i \in \mathcal{IC} \cup \mathcal{BC}} \psi_i \chi_i. \quad (36)$$

One can directly derive the stream function from the PV by solving a discrete elliptic BVP, which is a FV discretization of the continuous BVP (7),

$$\begin{cases} \frac{g}{f_0} [\Delta_h \psi_h]_i - \frac{f_0}{H} \psi_i = q_i - \beta y - \frac{f_0}{H} b_i, & i \in \mathcal{IC}, \\ \psi_i = \text{constant} & i \in \mathcal{BC}, \\ \sum_{i \in \mathcal{IC} \cup \mathcal{BC}} \psi_i A_i = 0. \end{cases} \quad (37)$$

We note that the BC (7b) and the constraint (7c) are enforced explicitly. This discrete system can be solved using the procedure outlined in (8)–(11).

The velocity field  $\mathbf{u}$  in the QG system is non-divergent, thanks to (1c). As a result, the nonlinear advection term in the transport equation (1a) can be written as a net flux of the PV  $q$ . With the discrete PV  $q_h$  defined at the cell centers, the most natural way to compute its fluxes is to define the normal velocity components at cell edges and use the discrete divergence theorem. According to (1c), the normal velocity component  $u_e$  can be computed using the stream function defined at the cell vertices. Therefore, to compute the velocity field  $\mathbf{u}_h$ , we first map  $\psi_h$  to a scalar field  $\tilde{\psi}_h$  on the cell vertices via (19),

$$\tilde{\psi}_h = [\widetilde{\psi_h}]. \quad (38)$$

The discrete velocity field is then computed using the discrete skewed gradient operator defined in (25)

$$\mathbf{u}_h = \sum_{e \in \mathcal{IE} \cup \mathcal{BE}} u_e \chi_e \mathbf{n}_e \quad (39a)$$

$$= \tilde{\nabla}_h^\perp \tilde{\psi}_h. \quad (39b)$$

The placement of these discrete variables is shown on Figure 4 in details. We recall that the PV  $q_h$  is the only prognostic variable, and the rest are all diagnostic variables, and can be computed (or diagnosed) from the prognostic variables. The discrete PV field evolves according to the following semi-discrete equation,

$$\frac{dq_i}{dt} + [\nabla_h \cdot (\mathbf{u}_h \hat{q}_h)]_i = \frac{1}{H} [\nabla \times \boldsymbol{\tau}]_i - \alpha \zeta_i, \quad i \in \mathcal{IC} \cup \mathcal{BC}. \quad (40)$$

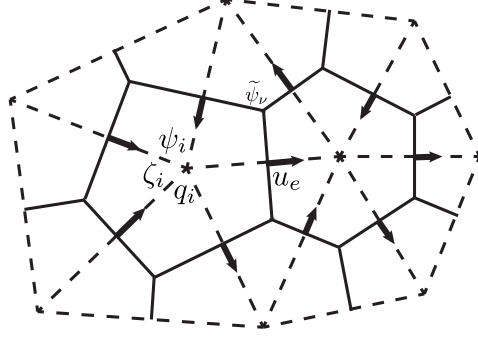


**Fig. 4** Placement of the discrete variables.

In the above,  $[\nabla \times \boldsymbol{\tau}]_i$  represents the value of the curl of the external forcing (wind) on cell  $i$ , which is calculated from the given function or data, and  $\widehat{q}_h$ , the discrete PV field at the cell edges, is a diagnostic variable computed from  $q_h$  by the cell-to-edge mapping (20),

$$\widehat{q}_h = [\widehat{q}_h] = \sum_{e \in \mathcal{IE} \cup \mathcal{BE}} \widehat{q}_e \chi_e. \quad (41)$$

The discrete relative vorticity is collocated with the PV  $q_h$  and the stream function  $\psi_h$ . It can be computed from the PV  $q_h$ , using the equation (7a),

$$\zeta_h = \sum_{i \in \mathcal{IC} \cup \mathcal{BC}} \zeta_i \chi_i, \quad (42a)$$

$$\zeta_i = q_i - \beta y_i + \frac{f_0}{H} (\psi_i - b_i). \quad (42b)$$

The advantage of this scheme is that the theoretical BC's (7b) and (7c) are enforced explicitly, and no artificial BC's are enforced or implied. The downside of this scheme is that, by discretizing the elliptic equation (7a) up to the boundary, it assumes that it holds up to the boundary, which is only possible if the stream function is smooth over the entire domain (i.e.  $C^2(\overline{\mathcal{M}})$ ). The last requirement is unusually high in theoretical analysis of this type of problems.

In summary, the FV scheme IVFV1 for the inviscid QG equation consists of the semi-discrete equation (40) and the auxiliary equations (37), (38), (39), (41), and (42).

#### 4.1.2 A FV scheme with artificial boundary conditions for the inviscid QG equation (IVFV2)

The previous numerical scheme IVFV1 leaves the PV  $q_h$  freely advected by the velocity field, even on the boundary. The boundary conditions are applied on the stream function only, and they affect the evolution of the PV  $q_h$  through the stream function. No explicit constraints are imposed on the boundary

values of the PV. To maintain some control on the boundary behavior of the PV, an artificial BC can be utilized. For the inviscid flow and *in the absence of external forcing near the boundary*, the fluids there will flow along the boundary, and there should be no velocity differential in the immediate vicinity of the boundary. We consider a partial cell on the boundary (Figure 5). We imagine that the partial cell is completed by a ghost partial cell (dashed) through mirroring. Then the cell center of the original partial cell becomes the center of the whole cell. Within this cell and near the boundary, due to the constraint exerted by the rigid but frictionless boundary, the flow has a uniform velocity along the direction of the boundary. Thus, at the cell center, the vorticity should be zero identically. The same conclusion will result when one project the velocity field onto the edges, and then apply Green's theorem on the tangential velocity components around the cell (red arrows). Thus, we propose the following BC for the relative vorticity,

$$\zeta_i = 0, \quad i \in \mathcal{BC}. \quad (43)$$

For the PV, this condition implies that

$$q_i = \beta y_i - \frac{f_0}{H} (\psi_i - b_i), \quad i \in \mathcal{BC}. \quad (44)$$

Physically, the condition (44) means that, on the boundary, the PV equals the local planetary vorticity plus the variations in the top surface and the bottom topography. Both the planetary vorticity and the bottom topography are fixed in time; only the top surface is time dependent.

Near the boundary, the velocity component along the boundary is given by  $\partial\psi/\partial\mathbf{n}$ , and the vorticity is given by  $\partial^2\psi/\partial\mathbf{n}^2$ , where  $\mathbf{n}$  designates the outer normal unit vector on the boundary. Thus, in terms of the continuous variables, the artificial BC (43) means that

$$\frac{\partial^2\psi}{\partial\mathbf{n}^2} = 0, \quad \text{on } \partial\mathcal{M}. \quad (45)$$

Geometrically, this condition mandates that, near the boundary, the stream function be linear along the direction normal to the boundary (Figure 6). *We point out that this BC is unphysical, not needed by the continuous system, and it cannot be supported either.* But its discrete version, namely (43) and (44), can help to exert a certain amount of control on the behavior of the PV on the boundary.

The rest of the scheme will remain the same as the previous scheme, except that the scope of the indices for certain equations (40) need to be adjusted to reflect the newly imposed BC's. Specifically, the discrete equation (40) is changed to

$$\frac{dq_i}{dt} + [\nabla_h \cdot (\mathbf{u}_h \hat{q}_h)]_i = \frac{1}{H} [\nabla \times \boldsymbol{\tau}]_i - \alpha \zeta_i, \quad i \in \mathcal{IC}, \quad (46)$$



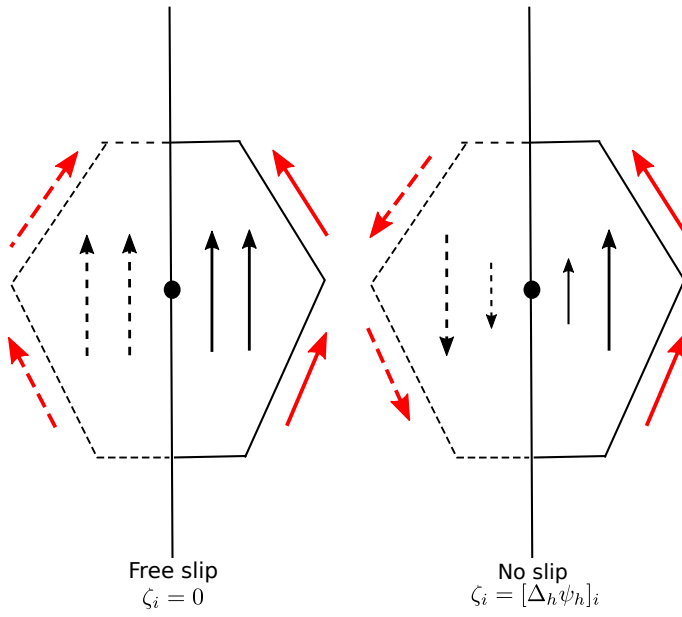


**Fig. 5** Boundary conditions on the vorticity.

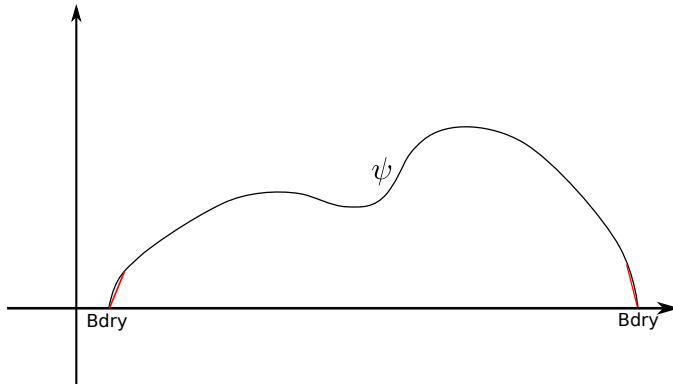


**Fig. 6** Artificial boundary conditions on  $\psi$ .

and the equation (42b) is changed to

$$\zeta_i = q_i - \beta y_i + \frac{f_0}{H} (\psi_i - b_i), \quad i \in \mathcal{IC} \quad (47)$$

for computing the vorticity in interior cells.

In summary, the FV scheme with an artificial boundary condition for the inviscid QG equation consists of the semi-discrete equation (46) and the auxiliary equations (37), (38), (39), (43), (44), (41), and (47).

## 4.2 Finite volume schemes for the viscous QG equation

The viscous QG equation (1) with a non-zero viscosity  $\mu$  requires two boundary conditions (3) and (5) plus one constraint (13)<sub>4</sub>. It has been pointed out in Section 2 that, if one wants to determine the stream function  $\psi$  from the PV  $q$ , one needs to differentiate the elliptic equation (1b) to obtain a fourth-order biharmonic equation so that the full boundary conditions can be enforced. However, doing so will kill the beta term in the specification of the PV  $q$ , and will have a detrimental impact on the dynamical behavior of the system. Numerical tests have demonstrated that this approach leads to an over-diffusive system, and that the phenomenon that relies on the beta effect, namely the intensification of the western boundary current, is largely gone. To remedy this issue, we propose two different approaches.

### 4.2.1 A semi-implicit finite volume scheme for the viscous QG equation (VSFV1)

The first approach is to skip the intermediate step on the PV advection, and solve for the stream function from a semi-implicit discretization of the fourth-order equation (1a) directly. As before, the stream function  $\psi$  is approximated by a discrete scalar field  $\psi_h$  defined at the cell centers. From the discrete stream function  $\psi_h$ , the discrete relative vorticity  $\zeta_h$  can be fully expressed on the interior cells,

$$\zeta_i = [\Delta_h \psi_h]_i, \quad i \in \mathcal{IC}. \quad (48)$$

The PV  $q_h$  is also fully expressed on the interior cells, according to (1b) and (1d),

$$q_i = [\Delta_h \psi_h]_i + \beta y_i - \frac{f_0}{H}(\psi_i - b_i), \quad i \in \mathcal{IC}. \quad (49)$$

The diffusion  $\Delta \zeta$  can be expressed on the interior cells that are not connected to any boundary cells as

$$[\Delta_h \zeta_h]_i = [\Delta_h^2 \psi_h]_i, \quad i \in \mathcal{IC} \setminus \mathcal{BC}1. \quad (50)$$

To obtain the discrete velocity field, one first maps the stream function  $\psi_h$  to a discrete scalar field  $\tilde{\psi}_h$  defined at the cell vertices via (38). The discrete vector field representing the velocity is given by (39b).

Substituting the above expressions for  $q_i$ ,  $\zeta_i$ ,  $[\Delta_h \zeta_h]_i$  and  $\mathbf{u}_h$  into the equation (1a), one obtains a semi-discrete scheme,

$$\begin{aligned} \frac{d}{dt} \left( [\Delta_h \psi_h]_i + \beta y_i - \frac{f_0}{H}(\psi_i - b_i) \right) + [\nabla_h \cdot (\mathbf{u}_h \hat{q}_h)]_i = \\ \frac{1}{H} [\nabla \times \boldsymbol{\tau}]_i - \alpha [\Delta_h \psi_h]_i + \mu [\Delta_h^2 \psi_h]_i, \quad i \in \mathcal{IC} \setminus \mathcal{BC}1. \end{aligned} \quad (51)$$

We note that, in order to be able to explicitly enforce the boundary conditions (3) and (5), we need to treat the (discrete) fourth order terms as unknowns. Thus, we discretize (51) by the semi-implicit Euler scheme,

$$\begin{aligned} \frac{1}{\Delta t} \left( [\Delta_h \psi_h^{n+1}]_i - \frac{f_0}{H} \psi_i^{n+1} - [\Delta_h \psi_h^n]_i + \frac{f_0}{H} \psi_i^n \right) + [\nabla_h \cdot (\mathbf{u}_h^n \hat{q}_h^n)]_i = \\ \frac{1}{H} [\nabla \times \boldsymbol{\tau}^{n+1}]_i - \alpha [\Delta_h \psi_h^{n+1}]_i + \mu [\Delta_h^2 \psi_h^{n+1}]_i \quad i \in \mathcal{IC} \setminus \mathcal{BC}1. \end{aligned}$$

Moving all the unknowns (i.e., the  $(n+1)$ th-step unknown variables) to the left-hand side of the equation, and the rest to the right-hand side, we obtain

$$\begin{aligned} -\mu \Delta t \frac{g}{f_0} [\Delta_h^2 \psi_h^{n+1}]_i + (1 + \alpha \Delta t) \frac{g}{f_0} [\Delta_h \psi_h^{n+1}]_i - \frac{f_0}{H} \psi_i^{n+1} = \frac{\Delta t}{H} [\nabla \times \boldsymbol{\tau}^{n+1}]_i - \\ \Delta t [\nabla_h \cdot (\mathbf{u}_h^n \hat{q}_h^n)]_i + \frac{g}{f_0} [\Delta_h \psi_h^n]_i - \frac{f_0}{H} \psi_i^n. \quad i \in \mathcal{IC} \setminus \mathcal{BC}1. \quad (52) \end{aligned}$$

We emphasize that the discrete equations (52) are only for interior cells not connected to any boundary cells. Additional equations or constraints are needed to complete the system, and they are supplied by discretizations of the boundary conditions (3), (5), and the constraint (13)<sub>4</sub>. The boundary condition (3) is discretized as

$$\psi_i^{n+1} = l, \quad i \in \mathcal{BC}, \quad (53)$$

where, for each time step,  $l$  is an unknown scalar value. The BC (5) can be discretized by specifying that the stream function on the cells next to the boundary cells by assuming the same scalar value as on the boundary cells,

$$\psi_i^{n+1} = l, \quad i \in \mathcal{BC}1. \quad (54)$$

Finally, the constraint (13)<sub>4</sub> is implemented by requiring the area weighted sum of the stream function be zero,

$$\sum_{i \in \mathcal{IC} \cup \mathcal{BC}} A_i \psi_i = 0. \quad (55)$$

To summarize, the semi-implicit numerical scheme for the viscous QG equation consists of (52), (53), (54), and (55). The main advantage of this approach is that the BC's are enforced explicitly and in a clean way. The main disadvantage is that the discretization of the fourth-order biharmonic operator results in a scheme with a stencil that is 2-3 times larger than the stencil of a second-order elliptic operator, making the scheme more expensive to solve.

#### 4.2.2 An explicit FV scheme for the viscous QG equation (VSFV2)

While the atmospheric and oceanic flows are considered viscous, the viscosity is extremely small. For example, in the interior of the world ocean, the flow has a Reynolds number on the order of  $10^{20}$  ([8]). Even though it is small, it would be a mistake to simply ignore the viscosity, for numerical and dynamical reasons. In fact, in the boundary layer region, both the length scale of the flow and the Reynolds are much smaller than they are in the interior of the domain, rendering the viscous terms dynamically significant. On the other hand, as pointed out in the previous subsection, incorporating the viscous terms implicitly in the solution process can be costly. In this subsection, we introduce a new scheme that is partly viscous and partly non-viscous. The viscosity is included, *explicitly*, in the PV advection. But it is not included when the stream function is computed from the PV.

As before, we approximate the PV  $q$  and the stream function  $\psi$  with the cell-centered discrete scalar fields  $q_h$  and  $\psi_h$ , respectively. Once the PV  $q_h$  is known, the stream function  $\psi_h$  is computed from a discrete elliptic BVP,

$$\begin{cases} \frac{g}{f_0} [\Delta_h \psi_h]_i - \frac{f_0}{H} \psi_i = q_i - \beta y_i - \frac{f_0}{H} b_i, & i \in \mathcal{IC}, \\ \psi_i = l & i \in \mathcal{BC}, \\ \sum_{i \in \mathcal{IC} \cup \mathcal{BC}} \psi_i A_i = 0. \end{cases} \quad (56)$$

We note that, while the continuous viscous QG equation requires two boundary conditions, only one of the BC's, i.e. (3), is explicitly enforced in the computation of  $\psi_h$ . In other words, the flow is simply treated as inviscid as far as the stream function is concerned. The stream function  $\psi_h$  is then mapped to a scalar field defined at cell vertices

$$\tilde{\psi}_h = [\widetilde{\psi_h}]. \quad (57)$$

A discrete vector field representing the normal velocity components at cell edges is computed from  $\psi_h$  by

$$\mathbf{u}_h = \tilde{\nabla}_h^\perp \tilde{\psi}_h. \quad (58)$$

A discrete scalar field representing the vorticity is needed for computing both the drag term and the diffusion term in (1a). The discrete vorticity is computed as

$$\zeta_h = \sum_{i \in \mathcal{IC} \cup \mathcal{BC}} \zeta_i \chi_i, \quad (59a)$$

$$\zeta_i = [\Delta_h \psi_h]_i, \quad i \in \mathcal{IC} \cup \mathcal{BC}. \quad (59b)$$

What distinguishes (59) from (48) is the range for the indices. The equation (48) is for interior cells that are not connected to any boundary cells, while the formula (59) is for all cells. The specifications (21), (26), and (30) of

relevant discrete differential operators make it clear that the discrete Laplacian operator is defined for all (interior and boundary) cells. It has been noted in the comment following equation (26) that a no-flux condition is implied on the boundary, because the edges along the domain boundary are not included in the calculation of the discrete divergence field. Hence, by computing the vorticity over the entire domain with the formula (59), we implicitly enforce the no-slip boundary condition (5),

$$\frac{\partial \psi}{\partial n} = 0, \quad \text{on } \partial \mathcal{M},$$

which is required for the continuous viscous QG equation.

With the no-slip boundary condition implicitly enforced in the calculation of the vorticity, it makes sense to update the PV on the boundary

$$q_i = \zeta_i + \beta y_i - \frac{f_0}{H} (\psi_i - b_i), \quad i \in \mathcal{BC}. \quad (60)$$

The updated PV field is then used for computing the PV on the cell edges

$$\widehat{q}_h = \widehat{[q_h]}. \quad (61)$$

Finally, the PV evolves according to the semi-discrete equation

$$\frac{dq_i}{dt} + [\nabla_h \cdot (\mathbf{u}_h \widehat{q}_h)]_i = \frac{1}{H} [\nabla \times \boldsymbol{\tau}]_i - \alpha \zeta_i + \mu [\Delta_h \zeta_h]_i, \quad i \in \mathcal{IC}, \quad (62)$$

We note that the diffusion is included in the above explicitly. Since the diffusion is only computed for the interior cells, no artificial or non-physical boundary conditions are explicitly or implicitly enforced on the vorticity.

## 5 Analysis on numerical transport of the PV

We here deal with the properties of an essential component of three out of the four schemes presented in the previous section, namely the numerical transport of the PV. Rigorous numerical analysis of these schemes, concerning their stability and convergence, will be left for future work.

The PV plays a central role in geophysical fluid dynamics ([21, 23]). Its importance stems from certain distinguishing properties that it enjoys. First, according to (1a), in the absence of the external forcing and the lateral and vertical diffusions, the PV is simply being transported by the velocity field. In other words, in the absence of the external forcing and the diffusions, the PV is preserved along the fluid paths. This property is of vital importance in the well-posedness analysis of the QG equation as well. Second, for predominantly two-dimensional large-scale geophysical flows, it is well known that the energy tends to concentrate at large scales (inverse energy cascade ([2, 19, 20])), and it is the (potential) enstrophy, i.e., the second moment of the (potential) vorticity, that cascades in the inertial range of the spectrum.

In the following we provide an analysis of the performance of the PV advection scheme on the PV dynamics and on the conservation of the potential enstrophy. For our analysis, all the external influences, such as the external forcing and the diffusions, have been dropped. Without these external factors, one will see that our pure advection scheme preserves the PV along the fluid paths in an averaging sense, and it also conserves the potential enstrophy up to the time truncation errors.

To evaluate the performance of the advection scheme on the PV dynamics, we start with the scheme (40). Substituting the specification (26) for the discrete divergence operator in the scheme and setting the external forcing  $\boldsymbol{\tau}$  and the bottom drag  $\alpha$  to zero, we obtain

$$\frac{d}{dt}q_i + \frac{1}{|A_i|} \sum_{e \in EC(i)} \widehat{q}_e u_e l_e n_{e,i} = 0, \quad i \in \mathcal{IC} \cup \mathcal{BC}. \quad (63)$$

Using the identity  $\widehat{q}_e = \widehat{q}_e - q_i + q_i$  in the above, we have

$$\frac{d}{dt}q_i + \frac{1}{|A_i|} \sum_{e \in EC(i)} (\widehat{q}_e - q_i) u_e l_e n_{e,i} + \frac{q_i}{|A_i|} \sum_{e \in EC(i)} u_e l_e n_{e,i} = 0, \quad i \in \mathcal{IC} \cup \mathcal{BC}. \quad (64)$$

We note that the last term on the left-hand side of (64) vanishes because it involves the discrete divergence of  $\mathbf{u}_h$ , which is divergence-free on every cell ([5]). We also note that  $\widehat{q}_e$ , computed via (41), is the arithmetic mean of  $q_i$  and the value of the PV on the cell on the other side of edge  $e$ , and  $\widehat{q}_e - q_i$  will simply be half of the difference between these two discrete PV values, and oriented outwards from cell  $i$ , i.e.

$$\widehat{q}_e - q_i = \frac{1}{2} d_e [\nabla_h q_h]_e n_{e,i}. \quad (65)$$

Substituting (65) in (64), we obtain

$$\frac{d}{dt}q_i + \frac{1}{|A_i|} \sum_{e \in EC(i)} \frac{1}{2} d_e l_e [\nabla_h q_h]_e u_e = 0, \quad i \in \mathcal{IC} \cup \mathcal{BC}. \quad (66)$$

Noticing that, for the diamond-shaped region,

$$A_e = \frac{1}{2} d_e l_e,$$

we can write (66) as

$$\frac{d}{dt}q_i + \sum_{e \in EC(i)} \frac{|A_e|}{|A_i|} [\nabla_h q_h]_e u_e = 0, \quad i \in \mathcal{IC} \cup \mathcal{BC}. \quad (67)$$

Within the summation,  $[\nabla_h q_h]_e u_e$  is obviously an approximation of the inner product of the *normal* components of  $\nabla q$  and  $\mathbf{u}$  on the edge. For the centroidal

Voronoi tessellation meshes ([12,10]), two neighboring cell centers are equidistant to the edge between them, and, thus, the following identity holds,

$$|A_i| = \frac{1}{2} \sum_{e \in \mathcal{EC}(i)} |A_e| \quad \text{or} \quad \sum_{e \in \mathcal{EC}(i)} \frac{|A_e|}{|A_i|} = 2.$$

Therefore, the summation on the left-hand side of (67) is a linear convex combination of the discrete convections across the edges surrounding cell  $i$ . The factor 2 comes from the fact that only the *normal* components are represented in the linear combination.

In the absence of an external forcing and the diffusions, the potential enstrophy is conserved under the QG equation. This can be directly verified by multiplying (1a) with  $q$  and integrate over  $\mathcal{M}$ ,

$$\begin{aligned} \frac{d}{dt} \int_{\mathcal{M}} q^2 dx &= - \int_{\mathcal{M}} \mathbf{u} \cdot \nabla \frac{1}{2} q^2 dx \\ &= - \int_{\mathcal{M}} \nabla \cdot \left( \frac{1}{2} \mathbf{u} q^2 \right) dx \\ &= - \int_{\partial \mathcal{M}} \frac{1}{2} q^2 \mathbf{u} \cdot \mathbf{n} ds \\ &= 0. \end{aligned}$$

We now show that our PV convection scheme also conserves the potential enstrophy, up to the truncation errors in time. We again start with the scheme (40), and drop the external forcing and the bottom drag,

$$\frac{d}{dt} q_h + \nabla_h \cdot (\mathbf{u}_h \widehat{q}_h) = 0. \quad (68)$$

Taking the inner product of (68) with  $q_h$ , we have

$$\frac{d}{dt} (q_h, q_h)_{0,h} + (\nabla_h \cdot (\mathbf{u}_h \widehat{q}_h), q_h)_{0,h} = 0.$$

In the above, both  $(\cdot, \cdot)_{0,h}$  designate the inner product (31) of scalar fields on the primary mesh. Applying the discrete integration by parts formula (33) to the second term, we obtain

$$\frac{d}{dt} (q_h, q_h)_{0,h} - 2(\mathbf{u}_h \widehat{q}_h, \nabla_h q_h)_{0,h} = 0. \quad (69)$$

Here, the second  $(\cdot, \cdot)_{0,h}$  designates the inner product (32) of discrete normal vector fields on the edges. We note that  $\widehat{q}_h = \sum \widehat{q}_e \chi_e$ , and  $\widehat{q}_e$  is the arithmetic mean of the discrete PV values on the neighboring cells on edge  $e$ , and  $\nabla_h q_h = \sum [\nabla_h q_h]_e \chi_e \mathbf{n}_e$ , where  $[\nabla_h q_h]_e$  is the gradient between the discrete PV values on the neighboring cells on edge  $e$ . It is easy to see that,

$$\widehat{q}_h \nabla_h q_h = \sum_{e \in \mathcal{IE} \cup \mathcal{BE}} \frac{1}{2} [\nabla_h q_h]_e \chi_e \mathbf{n}_e \equiv \nabla_h \frac{1}{2} q_h^2.$$

Therefore, we can write (69) as

$$\frac{d}{dt}(q_h, q_h)_{0,h} - (\mathbf{u}_h, \nabla_h q_h^2)_{0,h} = 0. \quad (70)$$

Applying the integration by parts formula (33) again, we arrive at

$$\frac{d}{dt}(q_h, q_h)_{0,h} + (\nabla_h \cdot \mathbf{u}_h, q_h^2)_{0,h} = 0.$$

Thanks to the incompressibility of the discrete vector field  $\mathbf{u}_h$ , we have

$$\frac{d}{dt}(q_h, q_h)_{0,h} = 0.$$

The potential enstrophy is conserved up to the time discretization errors.

## 6 Numerical experiments

### 6.1 A test case with a freely-evolving circular flow

In the previous section we have shown that the transport part of our scheme *conserves the PV along the fluid path in the average sense, and conserves the potential enstrophy up to the time truncation error*. In order to evaluate the performance of the scheme in practical simulations where space averaging and time discretization errors are present, we apply the scheme to a freely-evolving circular flow with no external forcing, no diffusion or no bottom drag.

We consider one section of the mid-latitude northern Atlantic ocean. The initial state of the flow is given by

$$d = \sqrt{\frac{(\theta - \theta_c)^2}{\Delta\theta^2} + \frac{(\lambda - \lambda_c)^2}{\Delta\lambda^2}}$$

$$\psi(\lambda, \theta) = e^{-d^2} \times (1 - \tanh(20 * (d - 1.5)))$$

In the above,  $\theta_c = 0.5088$  and  $\lambda_c = -1.1$  are the latitude and longitude of the center point of the Atlantic section,  $\Delta\theta = .08688$ ,  $\Delta\lambda = .15$ . The tanh function is used to ensure that the initial stream function is flat (with one constant value) along the boundary of the domain. A plot of the domain and of the stream function is shown in Figure 7. This stream function produces a circular clockwise velocity field in the middle of the ocean, with the maximum speed of about .8m/s near the center, which is considered fast for oceanic flows. No external forcing or diffusion is applied, and the flow is allowed to evolve freely. The circular pattern will breakdown eventually, because of the irregular shape of the domain and because of the non-uniform Coriolis force.

A spherical centroidal Voronoi-Delaunay mesh of the domain with 186,168 primary Voronoi cells and 367,589 dual Delaunay triangles is used, and the mesh resolution gradually changes from 21km to 2km when getting closer and closer to the boundary. The numerical scheme (IVFV1) of Section 4.1.1 is used,



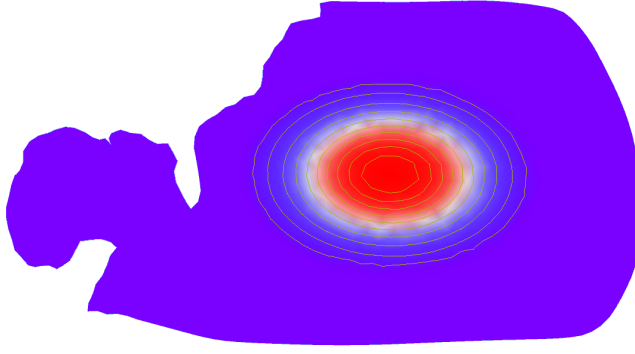


**Fig. 7** The initial stream function for a test of the pure PV advection scheme.

but with the external forcing and the bottom drag  $\alpha$  set to zero so that only the PV transport participates in the dynamics. A fourth-order Runge-Kutta scheme is used to discretize the equation (40). The model is run for 10 years, and the time step size is  $\Delta t = 1350s$ .

For this simulation, we want to see how well the PV and the potential enstrophy are conserved. For the QG equation, since the velocity field is incompressible, the PV satisfies the conservation laws. Due to the finite volume discretization technique used for the scheme, the PV is expected to be conserved both locally and globally. The global conservation of the PV is verified by a plot of the total PV against time (Figure 8 (a)). The total PV remains constant in time. Over the course of 10 years, the change in the total PV is only about  $1.25 \times 10^{-16}$  of the original total PV. Thus, under this scheme, the total PV is conserved up the machine errors.

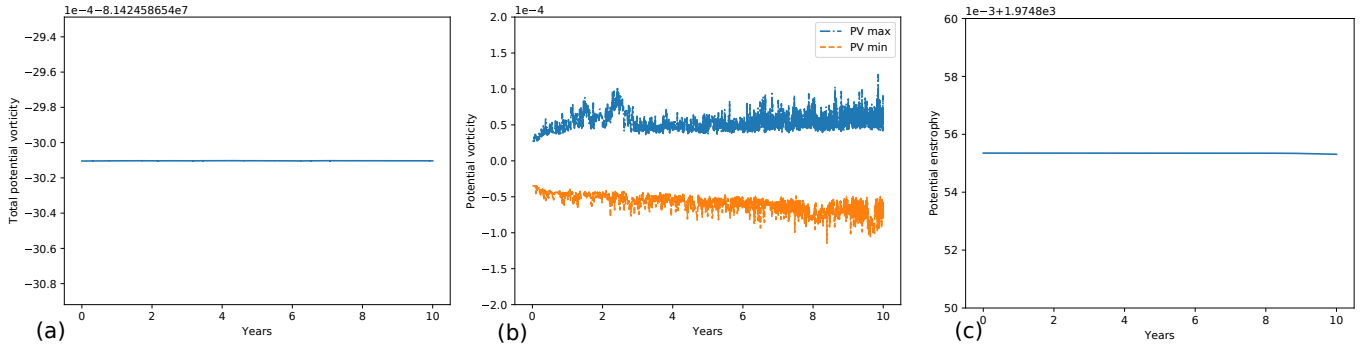


**Fig. 8** (a) Conservation of the total potential vorticity to the machine error. Over the course of 10 years, the change in the total potential vorticity is about  $1.25 \times 10^{-16}$  of the original total PV. (b) The evolution of the maximum and minimum values of the PV. (c) The conservation of the potential enstrophy. Over the course of 10 years, the change in the potential enstrophy is about  $3 \times 10^{-8}$  of the original potential enstrophy.

In the continuous system, the PV is also a quantity that is being transported by the velocity field, which means that, in the absence of an external forcing or diffusion, the PV is conserved along the fluid path. In the previous section, it has been shown that the transport component of our schemes conserve the PV along the fluid path in the averaging sense. From the discrete velocity field, it is impossible to fully reconstruct the fluid path, and therefore it is impossible to observe how PV evolves along any given fluid paths. Instead, we focus on the maximum value and the minimum values of the PV field. In the continuous system, since the PV is just being transported along the fluid particles, its maximum and minimum values will remain constant for all time. We want to know how well our scheme is able to preserve the maximum and minimum values of the PV field. However, it is not reasonable to expect the maximum and minimum values of the discrete PV are preserved exactly, because the scheme has only been shown to conserve the PV along the fluid path in the averaging sense. Oscillations are expected in the PV values, especially on the extreme values. In Figure 8(b), we plot the maximum and minimum values of the discrete PV against time. It can be seen the maximum and minimum values of the PV are not preserved exactly. They oscillate very fast, but they remain within some well-defined bounds. Initially, the PV values are within the interval of  $[-0.3 \times 10^{-4}, 0.3 \times 10^{-4}]$ , and throughout the entire simulation period of 10 years, the PV values remain within the bound of  $[-1.2 \times 10^{-4}, 1.2 \times 10^{-4}]$ .

Finally, we examine the performance of the scheme in conserving the potential enstrophy, which is the second moment of the PV. In Figure 8(c), we plot the potential enstrophy of the discrete system against time. The plot shows that the potential enstrophy remains largely constant in time. A close examination of the numerical values shows that, over the course of 10 years, the change in the potential enstrophy is about  $3 \times 10^{-8}$  of the initial potential enstrophy, which confirms that, under this scheme, the potential enstrophy is conserved up to the time discretization errors.

## 6.2 A test case with the intensified western boundary current

In this subsection, we numerically study the qualitative behaviors of all the schemes presented in Section 4, and identify the scheme that is most suitable for simulation of realistic flows in terms of both performance and efficiency.

To accomplish these goals, we utilize a test case that has much relevance to the realistic oceanic flows, namely a model for the intensified western boundary current, which, in the real world, takes the form of the Gulf stream, the Kuroshio current, the Brazilian current, etc. We consider the same section of the Atlantic ocean as in the previous section. But, here, the flow is initially at rest, and is being constantly driven by a zonally uniform wind stress of the form

$$\tau = \tau_0 \cos\left(\frac{\pi(\theta - \theta_0)}{\Delta\theta}\right),$$

where  $\tau_0 = 1.0 \times 10^{-4} \text{ m}^2/\text{s}^2$ ,  $\theta$  the latitude,  $\theta_0 \approx 15^\circ$  the latitude of the southern edge of the domain, and  $\Delta\theta \approx 30^\circ$  the latitudinal width of the domain. The wind stress has a negative curl, and thus is a source of negative vorticity to the flow.

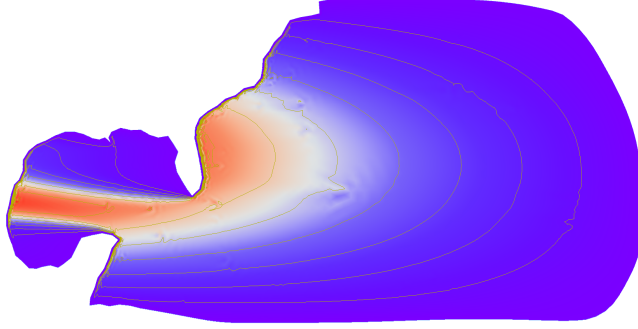


**Fig. 9** The solution (stream function) to the steady state linearized equation with a bottom drag  $\alpha = 5 \times 10^{-8}$  (the Stommel boundary layer) .

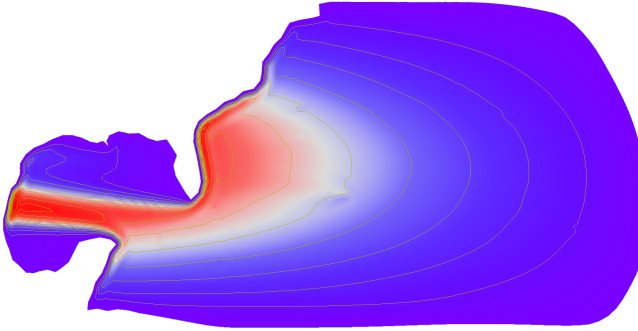


**Fig. 10** The solution (stream function) to the steady state linearized equation with a viscosity  $\mu = 100$  (the Munk boundary layer).

Stommel proposed the very first model ([31]) for the Gulf stream, articulating that the Gulf Stream is primarily the consequence of the anisotropic effect of the Coriolis force. What is the most surprising about Stommel's model is that the bottom drag, taking the same form as the zeroth order term on the right-hand side of (1a), is the only damping term, even though the Gulf stream has the appearance of a lateral boundary layer. When the lateral diffusion is included, the resulting boundary layer is called the Munk layer. Both the Stommel model and the Munk model are steady-state and linear. The solutions to these steady-state and linear models over the domain under consideration and

with the wind stress are plotted in Figures 9 and 10. These plots clearly show that the Stommel layer and the Munk layer share the same structure; they differ only in details near the western boundary. These steady-state solutions will serve as the reference solutions for the time-dependent solutions that we are about to compute.

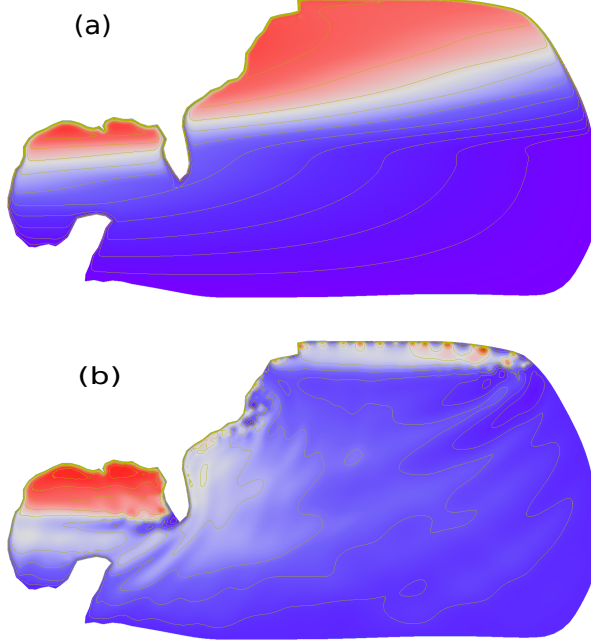


**Fig. 11** The stream functions at year 5, as computed with the FV schemes for the inviscid models. The flows are dissipated with only a bottom drag of  $\alpha = 5 \times 10^{-8}$ . Top: IVFV1; bottom: IVFV2.

In the inviscid model, the bottom drag is the only dissipative mechanism. In the previous Section, two schemes were proposed for this model. The scheme IVFV1 of Section 4.1.1 only enforces the BC (3) theoretically required for the model, while the scheme IVFV2 of Section 4.1.2 enforces the BC (3) and an extra artificial BC (45). Both schemes are applied to this test problem, with the bottom drag parameter  $\alpha = 5 \times 10^{-8}$ . The stream function computed using the scheme IVFV1, at the end of the 5-year simulation, is shown in Figure 11 (a). The domain is unmistakably divided into two regions, one with positive vorticity, and the other with flat stream function and (nearly) zero vorticity. In addition to the western boundary, the flow also exhibits intensified boundary currents at the northern and eastern boundaries. While this result is not a good reflection of the realistic oceanic flows, where the intensified boundary currents are only observed on the western boundary, it does confirm

an important principle for large-scale geophysical flows, namely that, in the absence of frictions, the PV tend to homogenize its self in the interior of the flow ([25]). The region with negative vorticity on the top is trying to offset the increase in the planetary vorticity in the flow.

With the artificial boundary condition (45) imposed by the scheme IVFV2, the homogenization process is disrupted. Since the relative vorticity is set to zero on the boundary and the surface fluctuations remain small, the PV on the boundary remain close to the planetary vorticity. This is approximately the case in reality (the planetary vorticity always dominates), and as a consequence, the stream function (Figure 11 (b)) is also much closer to those in Figures 9 and 10. The currents are only intensified near the western boundary. The stream of vortices on the top of the domain is the result of the combination of the free slip boundary condition and the vanishing curl of the wind stress there.

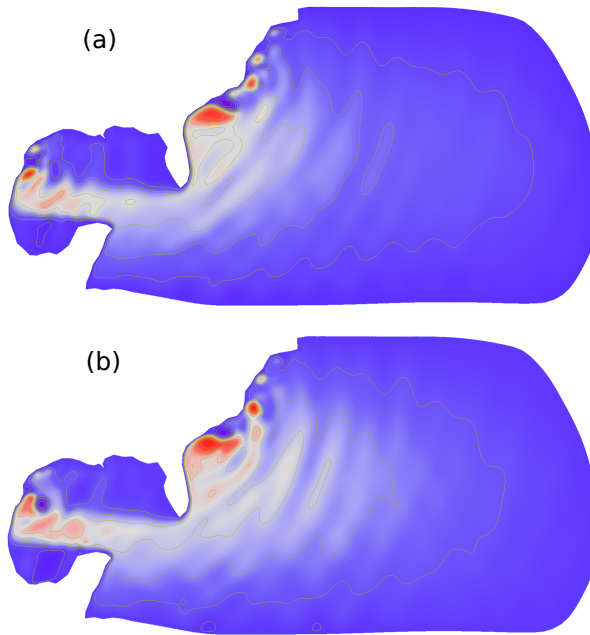


**Fig. 12** The stream functions at year 5, as computed with the FV schemes for the viscous models. The flows are dissipated with a bottom drag of  $\alpha = 3 \times 10^{-8}$  and a viscosity  $\mu = 40$ . Top: VSFV1; bottom: VSFV2.

When the lateral diffusion is included in the viscous model, the extra no-slip BC (5) is required for the continuous model. Both the BC's (3) and (5) are enforced explicitly in the semi-implicit scheme VSFV1, whereas the BC (5) is only implicitly enforced in the explicit scheme VSFV2. Both schemes are applied to this case, with a bottom drag  $\alpha = 3 \times 10^{-8}$ , and the lateral diffusion

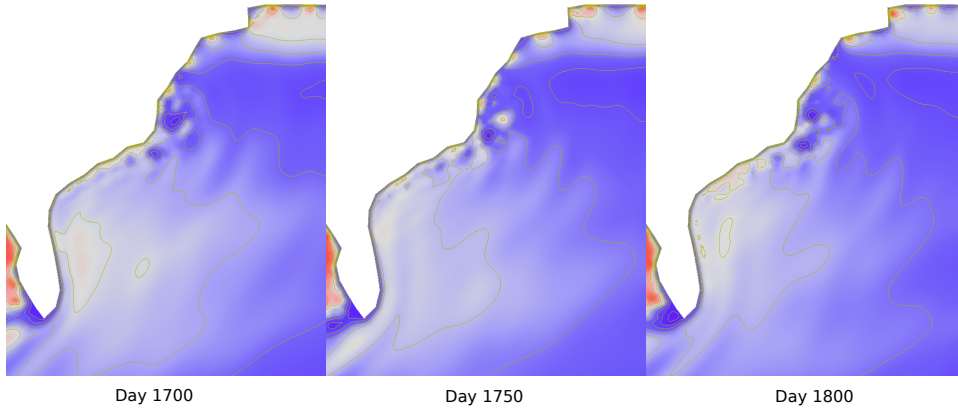


**Fig. 13** The stream functions, at days 1700, 1750, and 1800, with a bottom drag  $\alpha = 3 \times 10^{-8}$ , computed using IVFV1 and the Runge-Kutta 4th order scheme.

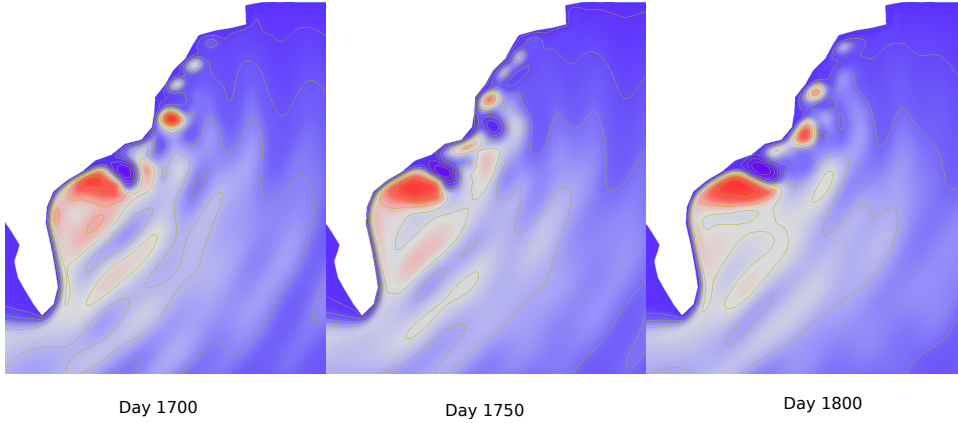


**Fig. 14** The stream functions, at days 1700, 1750, and 1800, with a bottom drag  $\alpha = 3 \times 10^{-8}$  and a viscosity  $\mu = 40$ , computed using VSFV1 and the semi-implicit Euler scheme.

$\mu = 40$ . The stream functions at the end of the 5-year simulation are plotted in Figure 12 (a) and (b). The stream functions from both schemes share the same large-scale structure of the steady-state Stommel-Munk boundary layers. Indeed, both schemes produce an intensified current near the western boundary only. The stream of vortices also disappear from the top of the domain, thanks to the no-slip boundary condition.

A comparison of the details in the boundary layer region is warranted in order to further distinguish these schemes. Presented in Figures 13, 14 and 15 are detailed views of the boundary layer region along the east coast of the United States for the schemes IVFV2, VSFV1, and VSFV2, respectively. IVFV1 is not included in this comparison because it does not produce a realistic rendering of the intensified western boundary current. These figures reveal

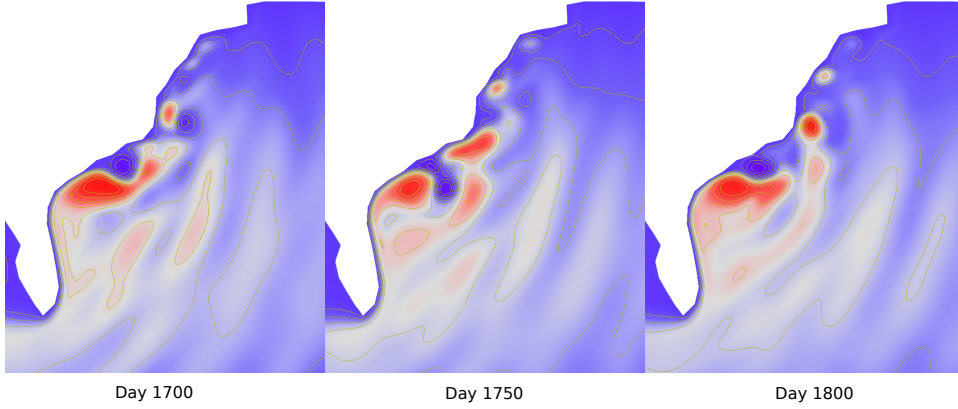


**Fig. 15** The stream functions, at days 1700, 1750, and 1800, with a bottom drag  $\alpha = 3 \times 10^{-8}$  and a viscosity  $\mu = 40$ , computed using VSFV2 and the Runge-Kutta 4th order scheme.

several aspects about these schemes. First, while the artificial BC (45) helps the scheme IVFV2 produce a stream function field that is close to that of the Stommel-Munk boundary layer, it also makes the boundary layer thinner than those produced by the scheme VSFV1 and VSFV2. Second, the artificial BC (45) also leads to subdued eddy activities in the boundary layer region, compared with those in Figure 14 and 15. Lastly, while the schemes VSFV1 and VSFV2 impose the theoretical BC (5) in different fashions, the boundary layers that they produce are of similar structures, with comparable width and eddy activity levels.

While the schemes VSFV1 and VSFV2 have similar dynamical behaviors, the scheme VSFV2, coupled with a higher-order explicit scheme such as the 4th order Runge-Kutta method, has significant efficiency advantages over the scheme VSFV1. The first advantage comes from the fact that the scheme VSFV2 only has to solve a second-order elliptic problem, while VSFV1 has to solve a fourth-order elliptic problem, which has a larger discrete stencil. Our simulation results indicate that solving a fourth-order elliptic PDE is more than twice as expensive as solving a second-order elliptic PDE. Another surprising and much more significant advantage of the scheme VSFV2 is that, with the 4th order Runge-Kutta method, it can use a comparable or larger time step size than the scheme VSFV1. This advantage can be attributed to the fact that the fourth-order Runge-Kutta method has a very large stability region. In our numerical tests, the scheme VSFV2 runs smoothly with a time step size of even 10800s, while the scheme VSFV1 can only use a time step size of 1200s. While using a different higher-order implicit time stepping technique may be able to ameliorate the efficiency for VSFV1, it is not expected that it can achieve the same performance as VSFV2.

## 7 Conclusions

The current work is part of the project to develop vorticity-divergence based numerical schemes for large-scale geophysical flows on arbitrarily unstructured primal-dual meshes over bounded domains. Vorticity-divergence based numerical schemes offer the optimal representations of the inertial-gravity wave relations, which are essential for an accurate simulation of the geostrophic adjustment process. They advance purely scalar quantities, i.e. the mass, vorticity, and divergence, and thus avoid the need for vector reconstructions, for which there is no satisfactory solutions yet on unstructured meshes. Finally, vorticity-divergence based numerical schemes, through the finite-volume finite-difference discretization techniques, offer the opportunity for a tighter control over such fundamental quantities as vorticity, and thus a more accurate simulation of the overall dynamics.

The current work concerns the barotropic QG equation with a free surface, which is a relatively simple model on the hierarchy of models for geophysical flows. Several finite volume schemes are presented for both the inviscid and the viscous equations. Great care is taken with regard to the specification of the boundary conditions. For the inviscid equation, a no-flux BC is required for the well-posedness of the model ([6]). We present a scheme (IVFV1) that implements this BC explicitly. But this scheme fails to produce a realistic rendering of the intensified western boundary current, due to the lack of control over the PV on the boundary. A second scheme (IVFV2) with an artificial free-slip BC is also presented. This scheme adds a certain level of control on the PV on the boundary by mandating that the vorticity be zero there. The rendering of the intensified western boundary current is improved, but, due to the free-slip condition, an unphysical stream of vortices appear along the northern boundary. The viscous model requires both no-flux and no-slip boundary conditions. Two schemes are proposed for this model as well. The scheme VSFV1 implements both the no-flux and no-slip BCs explicitly by using an semi-implicit time stepping scheme. The VSFV2 implements the no-flux BC explicitly, but the no-slip BC implicitly. Both schemes produce qualitatively similar results in the test involving the intensified western boundary currents. We find that the scheme VSFV2, coupled with the 4th order Runge-Kutta scheme, is significantly more efficient than the VSFV1 scheme. Realistic geophysical flows typically involve the lateral diffusion, usually in the form of eddy viscosity. The tests performed in this study show that, in these cases, the scheme VSFV2 should be used, as it can deliver the right dynamics at relatively little cost (compared with VSFV1). The scheme IVFV1, thanks to its clean implementation of the BC, is of theoretical interest, as it can be used in studies focusing on the inviscid nonlinear dynamics of the geophysical flows.

In subsequent works, we will consider more complex systems, such as the shallow water equations, the isopycnal models, etc. These system involve more prognostic and diagnostic variables, and it will be more challenging to find the right specifications for these variables so that certain quantities, e.g. the PV, the potential enstrophy etc., are conserved. As mentioned in the introduction,



in order for the vorticity-divergence based schemes to be appealing for practical applications, the performance of these schemes need to be further improved. The performance issue was skipped over all together in the current work, but will be dealt with in subsequent works. Our strategy for dealing with this issue will be a combination of iterative solvers, preconditioners, and good initial guesses.

**Acknowledgements** This work is partially supported by the Simons Foundation (contract number 319070) and by the US Department of Energy (grant number DE-SC0016540). We are also grateful to the referees whose comments helped improve the paper.

## References

1. Arakawa, A., Lamb, V.R.: Computational design of the basic dynamical processes of the UCLA General Circulation Model. *Methods in computational physics* **17**, 173–265 (1977)
2. Batchelor, G.K.: Computation of the Energy Spectrum in Homogeneous Two-Dimensional Turbulence. *Phys. Fluids* **12**(12), II–233–II–239 (1969)
3. Charney, J.G., Fjörtoft, R., Neumann, J.V.: Numerical integration of the barotropic vorticity equation. *Tellus* **2**(4), 237–254 (1950)
4. Chen, Q.: On staggering techniques and the non-staggered Z-grid scheme. *Numer. Math.* **132**(1), 1–21 (2016)
5. Chen, Q.: Stable and convergent approximation of two-dimensional vector fields on unstructured meshes. *J. Comput. Appl. Math.* **307**, 284–306 (2016)
6. Chen, Q.: The barotropic quasi-geostrophic equation under a free surface. (2017). Submitted
7. Chen, Q., Ringler, T., Gunzburger, M.: A co-volume scheme for the rotating shallow water equations on conforming non-orthogonal grids. *J. Comput. Phys.* **240**, 174–197 (2013)
8. Cushman-Roisin, B., Beckers, J.M.: Introduction to geophysical fluid dynamics: Physical and numerical aspects. Academic Press (2011)
9. Danilov, S.: On utility of triangular C-grid type discretization for numerical modeling of large-scale ocean flows. *Ocean Dyn.* **60**(6), 1361–1369 (2010)
10. Du, Q., Faber, V., Gunzburger, M.: Centroidal Voronoi tessellations: applications and algorithms. *SIAM Rev.* **41**(4), 637–676 (electronic) (1999)
11. Du, Q., Gunzburger, M.: Grid generation and optimization based on centroidal Voronoi tessellations. *Appl. Math. Comput.* **133**(2-3), 591–607 (2002)
12. Du, Q., Gunzburger, M.D., Ju, L.: Constrained centroidal Voronoi tessellations for surfaces. *SIAM J. Sci. Comput.* **24**(5), 1488–1506 (electronic) (2003)
13. Friedlander, S., Vicol, V.: Global well-posedness for an advection-diffusion equation arising in magneto-geostrophic dynamics. *Annales de l’Institut Henri Poincaré (C) Analyse Non Linéaire* **28**, 283–301 (2011)
14. Gassmann, A.: Inspection of hexagonal and triangular C-grid discretizations of the shallow water equations. *J. Comput. Phys.* **230**(7), 2706–2721 (2011)
15. Harlow, F.H., Welch, J.E.: Numerical Calculation of Time-Dependent Viscous Incompressible Flow of Fluid with Free Surface. *Phys. Fluids* **8**(12), 2182–2189 (1965)
16. Heikes, R., Randall, D.A.: Numerical integration of the shallow-water equations on a twisted icosahedral grid. Part I: Basic design and results of tests. *Mon. Weather Rev.* **123**(6), 1862–1880 (1995)
17. Heikes, R., Randall, D.A.: Numerical integration of the shallow-water equations on a twisted icosahedral grid. Part II. A detailed description of the grid and an analysis of numerical accuracy. *Mon. Weather Rev.* **123**(6), 1881–1887 (1995)
18. Ju, L., Ringler, T., Gunzburger, M.: Voronoi Tessellations and Their Application to Climate and Global Modeling. In: *Numerical Techniques for Global Atmospheric Models*, pp. 313–342. Springer Berlin Heidelberg, Berlin, Heidelberg (2011)

19. Kraichnan, R.H.: Inertial Ranges in Two-Dimensional Turbulence. *Phys. Fluids* **10**(7), 1417–1423 (1967)
20. Lilly, D.K.: Numerical simulation of Two-Dimensional turbulence. *The Physics of Fluids* **12**(12), II-240–II-249 (1969)
21. Lorenz, E.N.: Reflections on the Conception, Birth, and Childhood of Numerical Weather Prediction. *Annu. Rev. Earth Planet. Sci.* **34**(1), 37–45 (2006)
22. Majda, A.J., Wang, X.: Non-linear dynamics and statistical theories for basic geophysical flows. Cambridge University Press, Cambridge (2006)
23. Pedlosky, J.: Geophysical fluid dynamics, 2 edn. Springer (1987)
24. Randall, D.A.: Geostrophic adjustment and the finite-difference shallow-water equations. *Mon. Weather Rev.* **122**(6), 1371–1377 (1994)
25. Rhines, P.B., Young, W.R.: Homogenization of potential vorticity in planetary gyres. *J. Fluid Mech.* **122**, 347–367 (1982)
26. Ringler, T., Ju, L., Gunzburger, M.: A multiresolution method for climate system modeling: application of spherical centroidal Voronoi tessellations. *Ocean Dyn.* **58**, 475–498 (2008)
27. Ringler, T., Petersen, M., Higdon, R.L., Jacobsen, D., Jones, P.W., Maltrud, M.: A Multi-Resolution Approach to Global Ocean Modeling. *Ocean Model.* **69**, 211–232 (2013)
28. Ringler, T.D., Jacobsen, D., Gunzburger, M., Ju, L., Duda, M., Skamarock, W.: Exploring a multiresolution modeling approach within the shallow-water equations. *Mon. Weather Rev.* **139**(11), 3348–3368 (2011)
29. Ringler, T.D., Thuburn, J., Klemp, J.B., Skamarock, W.C.: A unified approach to energy conservation and potential vorticity dynamics for arbitrarily-structured C-grids. *J. Comput. Phys.* **229**(9), 3065–3090 (2010)
30. Skamarock, W.C., Klemp, J.B., Duda, M.G., Fowler, L.D., Park, S.H., Ringler, T.D.: A Multiscale Nonhydrostatic Atmospheric Model Using Centroidal Voronoi Tessellations and C-Grid Staggering. *Mon. Weather Rev.* **140**, 3090–3105 (2012)
31. Stommel, H.: The westward intensification of wind-driven ocean currents. *Eos Trans. Amer. Geophys. Union* **29**(2), 202–206 (1948)
32. Thuburn, J.: Numerical wave propagation on the hexagonal C-grid. *J. Comput. Phys.* **227**(11), 5836–5858 (2008)
33. Thuburn, J., Cotter, C.J., Dubos, T.: A mimetic, semi-implicit, forward-in-time, finite volume shallow water model: comparison of hexagonal-icosahedral and cubed-sphere grids. *Geoscientific Model Development* **7**(3), 909–929 (2014)